Novel organic semiconductors based on 2-amino-anthracene: Synthesis, charge transport and photo-conductive properties

Kirill Kondratenko, I. Carlescu, Pierre-Édouard Danjou, Yahia Boussoualem, Aurel Simion, Benoît Duponchel, Jean-François Blach, Christian Legrand, Nicolae Hurduc, Abdelylah Daoudi

PCCP

ARTICLE TYPE

Cite this: DOI: 00.0000/xxxxxxxxxx

Novel organic semiconductor based on 2-amino-anthracene: synthesis, charge transporting and photoconductive properties†

K. Kondratenko,*[a‡] I. Carlescu,[b] P.-E. Danjou,[c] Y. Boussoualem,[a] A. Simion,[b] B. Duponchel,[a] J.F. Blach,[d] C. Legrand,[a] N. Hurduc[b] and A. Daoudi[a]

Received Date
Accepted Date

DOI: 00.0000/xxxxxxxxxx

Anthracene is considered to be a popular choice as a building block for organic semiconductors. Present work is dedicated to synthesis and characterization of a novel semiconductor (**10-OPIA**) possessing mesogenic properties, which allows better control over charge transport in the bulk of material. Novel anthracene-based molecule is characterized for its potential applications: frontier molecular energy levels are studied by optical spectroscopy and cyclic voltammetry and confronted to values obtained via *ab initio* calculations. Thermophysical and mesogenic properties are investigated by optical microscopy and differential scanning calorimetry. Charge transporting properties are characterized by means of an OFET device. It is found that this material can be easily aligned and exhibits field effect hole mobility of $5.22 \times 10^{-5}\,\mathrm{cm^2/(V\,s)}$ and ON/OFF ratio of 10^4 in the device prepared by drop casting. Finally, photoconductive properties of this novel material are addressed in order to investigate its potential applications to organic phototransistors: it exhibits large photoconductive gain of >100 and photo-responsivity of $>1\,\mathrm{A/W}$.

1 Introduction

Organic electronics is a rapidly developing field of scientific research. In recent years, significant efforts have been devoted to development of organic semiconductors (OSCs) for applications such as field effect transistors (OFETs), light emitting diodes (OLEDs) and photovoltaics (OPVs). These substances posses developed π-conjugated structure which is the key to their charge transporting properties[1].

Historically, one of the first evidence of charge transport in organic molecules was discovered in anthracene crystals. Since then, enormous progress has been made, and many other molecules have been identified as promising organic semiconductors. Nevertheless, anthracene still attracts significant attention as a building block for the OSC materials.

Indeed, the anthracene molecule presents a vast array of opportunities as a building block: large diversity of symmetric and asymmetric derivatives in end- (2, 3, 6, 7) as well as peri- (1, 4, 5, 8, 9, 10) positions has been synthesized and their charge transporting properties investigated over last decades[2]. Many attempts were made to increase the size of π-conjugated backbone by attaching aromatic fragments symmetrically to end positions (phenyl[3], naphthalene[4], anthracene[5], thiophene[6], etc.).

These efforts have proven the great potential of anthracene based molecules, and in addition to improving charge transport, significant efforts were dedicated to facilitate processing of these materials. Use of (triisopropylsilyl)ethynyl (TIPS) functional groups is a remarkable example of improvement of solubility, with a (9,10)-TIPS-functionalized molecule substituted with naphthalene in 2,6-positions which attained hole mobility $\mu = 3.7\,\mathrm{cm^2/(V\,s)}$[7].

However the prerequisites which favor charge transport, such as strong $\pi - \pi$ overlap expected to increase transfer integral and improve charge hopping from site to site may seem often result in an insoluble material thus significantly limiting its potential applications. Certain structural features, such as alkyl chains, are able to improve solubility as well as grant mesogenic properties to the material, which provides unique opportunities to control its structural properties in the form of thin film[8]. However, designing of a mesogenic molecule with a reasonable mesophase temper-

[a] *Univ. Littoral Côte d'Opale, UR 4476 - UDSMM - Unité de Dynamique et Structure de Matériaux Moléculaires, 59140 Dunkerque, France; E-mail: kirill.kondratenko@univ-lille.fr*
[b] *Department of Natural and Synthetic Polymers, "Cristofor Simionescu" Faculty of Chemical Engineering and Environmental Protection, "Gheorghe Asachi" Technical University of Iasi, 700050 Iasi, Romania*
[c] *Univ. Littoral Côte d'Opale, UR 4492 - UCEIV - Unité de Chimie Environnementale et Interactions sur le Vivant, 59140 Dunkerque, France*
[d] *Univ. Artois, CNRS, Centrale Lille, ENSCL, Univ. Lille, UMR 8181, Unité de Catalyse et Chimie du Solide (UCCS), 62300 Lens, France*
† Electronic Supplementary Information (ESI) available. See DOI: 10.1039/cXCP00000x/
‡ Present address: Institut d'Electronique Microléctronique et Nanotechnologie (UMR 8520 IEMN), CNRS, 59652 Villeneuve d'Ascq, France

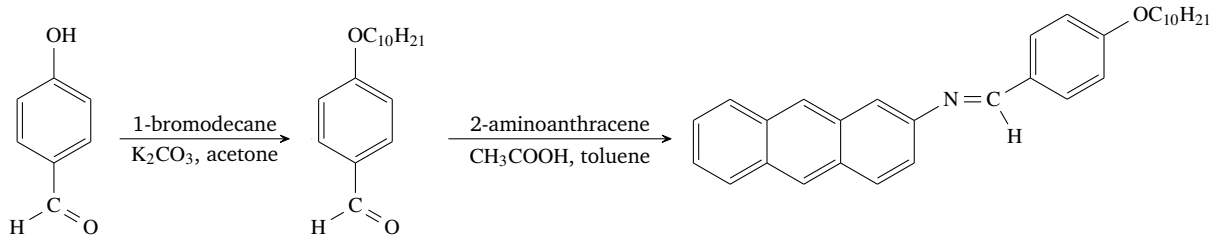

Fig. 1 Synthesis of **10-OPIA**.

ature range is not trivial. It is now of interest to address some anthracene-based liquid crystals which possess semiconducting properties. Meńy *et al.* have made a significant contribution to the investigation of 2,6-substituted anthracene derivatives[9]: it was found that direct attachment of flexible alkyl chains to the end positions of anthracene is not sufficient to obtain mesomorphic properties. Insertion of additional phenyl moieties between the anthracene and alkyl spacer has allowed not only to increase the overall flexibility of the molecule (which increases probability to attain mesomorphic properties), but to additionally increase the size of π-conjugated backbone. However, it is worth mentioning that hole mobility measured in Sm_C and Sm_A mesophases were of about $2\times10^{-3}\,\mathrm{cm^2/(V\,s)}$ at maximum, which is of the same order of value as for phenyl naphthalene derivative[10] in Sm_B mesophase. In addition to relatively small gain in hole mobility, the mesomorphic behaviour was exhibited on very high temperature ($>200\,^{\circ}$C).

An insoluble 2-substituted derivative of anthracene was prepared by Chen *et al.*[11], which in addition to p-type transporting properties exhibits photosensitivity due to incorporation of an azo-group. This substance has a relatively low mesophase transition temperature (about 140 °C), which makes it more convenient to investigate its charge transport. The cooperative effects of UV-irradiation (molecular structure rearrangement) and thermal annealing (crystalline order improvement) have resulted in mobility increase from $0.019\,\mathrm{cm^2/(V\,s)}$ to $0.746\,\mathrm{cm^2/(V\,s)}$.

We also wanted to explore the possibility of extending the π-conjugated backbone by employing imine linkage. This method can be less demanding than formation of carbon - carbon bonds by usual methods such as Suzuki coupling (which requires inert atmosphere, expensive precursors and catalysts). The purification of reaction products is also easier, as the only byproduct of the reaction is water[12]. The resulting imine is isoelectronic to vinylene linkage[13], which is commonly encountered in organic semiconductors.

In this work, we have developed an easy-to-synthesize semiconductor which is based on inexpensive and readily available precursors. We describe synthetic procedure and present some fundamental properties of the molecule: band gap energy, frontier molecular energy levels, thermo-physical properties. Charge transport is investigated by preparation of a field-effect transistor. Finally, we investigate photoconducting properties of the molecule in scope, which may be relevant for potential light-sensitive applications.

2 Experimental section

1-bromodecane and 2-aminoanthracene were purchased from Alfa Aesar, 4-hydroxy-benzaldehyde was purchased from Sigma Aldrich. All chemicals were used as received without further purification. NMR analysis was performed on Bruker Avance III 400 MHz spectrometer. Mass spectrum was recorded on Agilent 6540 UHD Q-TOF LC/MS system. DFT calculations were performed with the help of Gaussian 16, Rev. A03 software[14]. Optical absorption spectroscopy was performed on Perkin Elmer Lambda 2 spectrometer with dilute (10^{-5} M) solution in dichloromethane in a standard quartz cuvette with optical path of 1 cm on a range from 230 nm to 500 nm. Fluorescensce spectrum was obtained on Cary (Agilent) Eclipse spectrometer. Fluorescence decay was measured on Horiba DeltaFlex TCSPC Lifetime Fluorometer. Cyclic voltammetry was performed with Metrohm AUTOLAB PGSTAT302. 2 mmol/L solution of **10-OPIA** in dichloromethane containing 0.1 M of tetrabutylammonium hexafluorophosphate ($TBAPF_6$) as a supportive electrolyte was stirred for 2h and then placed in the electrochemical cell (10 ml volume). The solution was degassed by Ar bubbling for 20 minutes. Cyclic voltammograms were collected in the range from -2.2 to 1.8 V against silver wire pseudoreference with scanning speeds ranging from 50 to 500 mV/s. After collection of **10-OPIA** voltammograms, 2 ml of 1 mmol solution of ferrocene (98%, Sigma Aldrich) in supporting electrolyte was injected in the cell and degassed for 20 minutes prior to measurements. Additional data was recorded to include the potential range of Fc/Fc+ oxidation process. The data of ferrocene oxidation was further used to extract its half-wave potential (mean value between the anodic and cathodic peaks, since Fc/Fc+ process is quasi-reversible) and use it as a reference point[15] for the previously obtained data for **10-OPIA**. Differential scanning calorimetry (DSC) was performend on TA Instruments Q1000. Electrical emeasurements were performed with two Keysight B2901 SMUs.

2.1 Synthetic route

We have developed a new molecule ((E)-N-(anthracen-2-yl)-1-(4-(decyloxy)-phenyl)methanimine or **10-OPIA**, Figure 1) which can be prepared easily from commercially available materials: the phenyl moiety is attached to anthracene by an imine linkage which can be obtained by a simple nucleophilic addition between 2-aminoanthracene and 4-alkyloxy-benzaldehyde derivatives. The length of terminal flexible chain can be efficiently controlled by choosing an appropriate alkyl halide precursor.

Alkylation of 4-hydroxy-benzaldehyde

0.31 g (2.5 mmol) of 4-hydroxy-benzaldehyde was placed in a round bottom flask with 0.66 g (3 mmol) of 1-bromo-decane. 0.41 g (3 mmol) of K_2CO_3 was added to the reaction mixture. Finally, 15 ml of acetone were introduced, and the mixture was set to reflux with stirring for 48 h. After the reaction was finished, the acetone was evaporated under reduced pressure and the crude 4-decyloxy-benzaldehyde (**PDBA**, Figure 1) was purified by column chromathography with a mixture of dichloromethane and hexane $\sim$ 1:1 v/v ratio. This procedure allowed us to recover 0.53 g of **PDBA** which corresponds to 82% yield. ^{1}H-NMR (400 MHz, $CDCl_3$) δ = 9.87 (*s*, 1H); 7.81 (*d*, $J = 8.4$ Hz, 2H); 6.98 (*d*, $J = 8.3$ Hz, 2H); 4.03 (*t*, $J = 6.6$ Hz, 2H); 1.80 (*quint*, $J = 6.8$ Hz, 2H); 1.46 (*m*, 2H); 1.30 (*m*, 12H); 0.88 (*t*, $J = 6.9$ Hz, 3H) ppm (Figure 1 of ESI†).

Imine synthesis

0.53 g (2 mmol) of the purified **PDBA** with 0.39 (2 mmol) g of 2-amino-anthracene (**2-AA**) were placed in a round bottom flask. The initial products were dissolved in 25 ml of toluene, and a few drops of glacial acetic acid were introduced as a catalyst. The reaction mixture is allowed to reflux with stirring for 48 h. The final product precipitated from the reaction mixture upon cooling, and was filtered and washed with cold toluene and further with acetone to remove toluene. The crude **10-OPIA** was dried in the oven and then recrystallized in minimal amount of chloroform. Finally, we have obtained 0.55 g of **10-OPIA** which corresponds to 57% yield. ^{1}H-NMR (400 MHz, $CDCl_3$) δ = 8.58 (*s*, 1H); 8.41 (*d*, $J = 2.6$ Hz, 2H); 8.02 (*m*, 3H); 7.91 (*d*, $J = 8.7$ Hz, 2H); 7.70 (*d*, $J = 1.5$ Hz, 1H); 7.52-7.39 (*m*, 3H); 7.01 (*d*, $J = 8.7$ Hz, 2H); 4.04 (*t*, $J = 6.6$ Hz, 2H); 1.82 (*quint*, $J = 6.6$ Hz, 2H); 1.48 (*m*, 2H); 1.30 (*m*, 12H); 0.89 (*t*, $J = 6.9$ Hz, 3H) ppm. ^{13}C-NMR (100 MHz, $CDCl_3$) δ = 162.1, 159.8, 149.6, 132.5, 132.2, 131.5, 130.8, 130.5, 129.4, 129.2, 128.4, 128.1, 126.3, 126.1, 125.7, 125.2, 122.2, 117.0, 114.9, 68.4, 32.1, 29.7, 29.6, 29.5, 29.3, 26.2, 22.8, 14.3 ppm. ^{1}H and ^{13}C NMR spectra are shown in Figures 2 (a) and (b) of ESI†. HRMS (ESI+Q-TOF) calculated for $[C31H36NO]^+$ 438.2791, found 438.2790. This molecule is stable in solid state: we have compared the NMR spectra after 8 months of storage in ambient conditions and no traces of degradation were detected.

Device fabrication

The OFET devices in bottom gate - bottom contact were fabricated by utilizing commercially available substrates provided by Ossila (Sheffield, UK) fabricated on heavily doped silicon wafer with thermally grown SiO_2 (300 nm) as gate insulator and evaporated Au source and drain contacts. Before deposition, substrates were washed with Decon™ 90 solution, deionized water, acetone and isopropanol for 5 mins in succession. The substrates were further subjected to UV-Ozone cleaning for 20 min. The channel dielectric layer (SiO_2) was functionalized with self-assembled monolayer (SAM) of octadecyltrichlorosilane (OTS-18) solution in hexadecane for 30 min, then substrates were washed with chloroform. The semiconductor was deposited by drop-casting from 0.5% chlorobenzene solution on inclined substrate in saturated vapor conditions in order to obtained ordered films. Hole mobility was calculated from source-drain current I_{DS} in saturation regime by using the following equation:

$$I_{DS} = \left(\frac{W}{2L}\right) \mu_F C_i \left(V_{GS} - V_{th}\right)^2, \quad (1)$$

where W is the channel width and L is the channel length, C_i is the capacitance per unit area of the gate dielectric, μ_F is the field-effect mobility and V_{th} is the threshold voltage.

3 Results and discussion

DFT computation of molecular structure

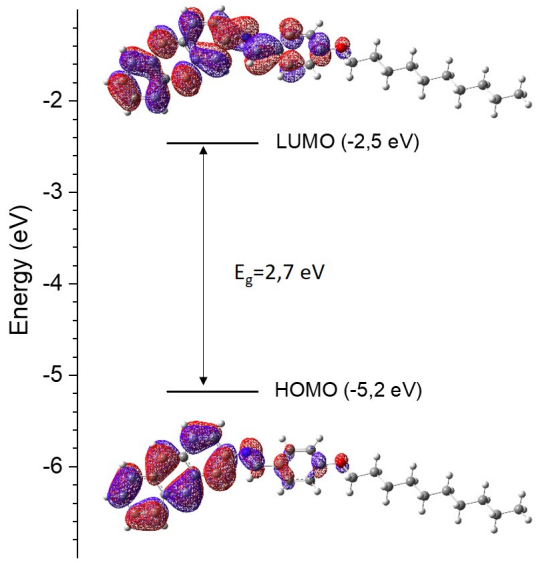

Fig. 2 Frontier molecular orbitals of the **10-OPIA** molecule, calculated on B3LYP/6-31G++(d,p) level. MO energy levels are extracted from cyclic voltammetry data.

Molecular geometry of **10-OPIA** was obtained through DFT optimization at B3LYP/6-31G++(d,p) level of theory. Optimized structure had zero imaginary frequencies. Calculated geometries of frontier molecular orbitals are presented in the Figure 2. It is of interest to note the distribution of electron density over $\pi-$conjugated backbone: the HOMO of this molecule seems to be mostly localized on the electron-rich anthracenyl moiety. The initial estimation of the band gap (3.3 eV) is performed by subtracting calculated energy levels of HOMO (-5.3 eV) and LUMO (-2.0 eV). The close proximity of HOMO energy level (-5.3 eV) to the work function ϕ of Au (about -5.1 eV) allows us to expect shallow barrier for hole injection from the Au electrode, as well as ambient air stability due to its deep localization.

We have further investigated electronic properties of **10-OPIA** molecule by optical spectroscopy and cyclic voltammetry. Characterization of thermophysical and mesogenic properties can be found in ESI†.

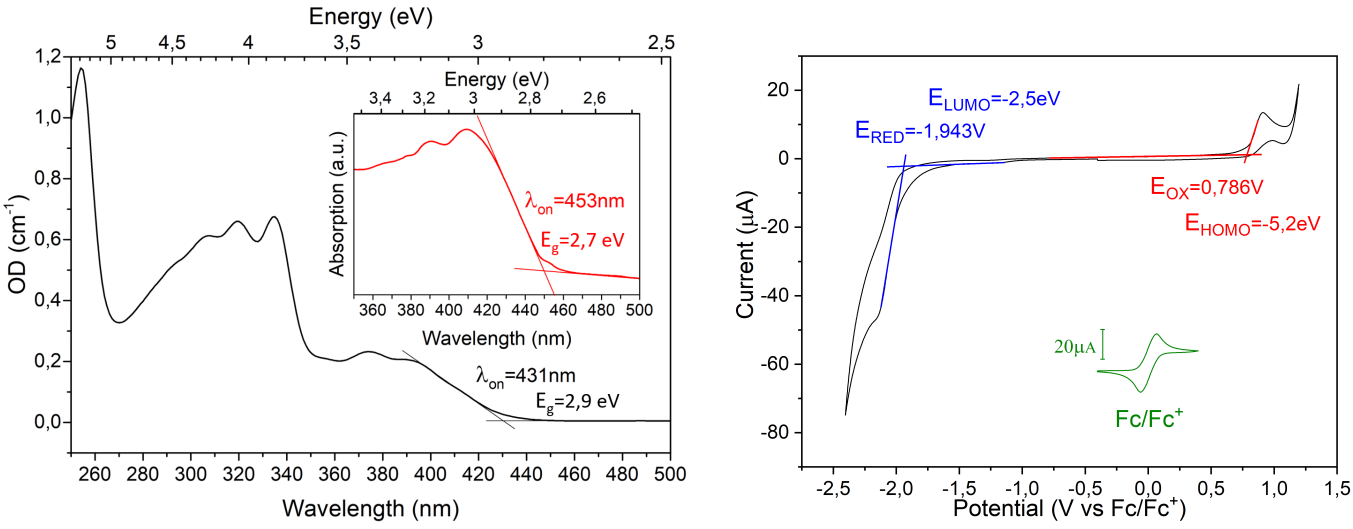

(a) (b)

Fig. 3 (a) Absorption spectra of **10-OPIA** in dichloromethane solution. **Inset:** Absorption spectrum in thin film form. (b) Cyclic voltammograms of **10-OPIA** solution and Fc/Fc+ reference (vertical offset added for clarity).

Optical spectroscopy

Optical band gap, corresponding to the first electronic transition ($S_0 \rightarrow S_1$, HOMO $\rightarrow$ LUMO) was extracted from the onset of optical absorption by drawing a tangent at the first absorption band, as illustrated in Figure 3, (a).

Absorption spectrum in solid state was recorded for a thin film of **10-OPIA** which was deposited on a quartz slide by drop-casting. It was found that **10-OPIA** exhibits a red shift of 22 nm when in thin film (inset of Figure 3, a), which may be explained by more pronounced $\pi-\pi$ interactions of neighboring molecules in the crystalline phase as opposed to that of in solution, which results in a band gap energy reduction for the bulk **10-OPIA**.

By utilizing the relation $E = \frac{hc}{\lambda}$, where E is the energy, h is the Planck's constant and λ is the wavelength; the optical band gap is calculated to be E_g = 2.9 eV for the onset of absorption of 431 nm in dichloromethane solution, and E_g = 2.7 eV for the onset of absorption of 453 nm in the form of solid thin film, respectively. Both of these values are noticeably smaller than initial estimation from *ab initio* calculations.

It is well-known that compounds containing imine linkage show little to no light emitting properties [12]. However, 10^{-5} M solution of **10-OPIA** in acetone (degassed by freeze-pump-thaw method on a Schlenck line) was weakly fluorescent (Figure 5 (a) of ESI†). Emission peak is situated at 480 nm (excitation wavelength - 435 nm). Similarly, fluorescence lifetime measurements were carried out in acetone solution with excitation at 370 nm. Unusually high lifetime (9.44 ns) indicates some hindering of the rotation around imine linkage axis, which is the preferred way of non-radiative relaxation for this type of materials. Possible reasons include interaction between lone electron pair on the nitrogen atom and anthracenyl π−conjugated system due to nonplanar geometry of the molecule (dihedral angle between anthracenyl and phenyl structures is about 140°). Similar effect was observed by Yoshino *et al.* [16] for molecules with constrained azo- and imine linkages, which resulted in enhancement of fluorescence.

Cyclic voltammetry

Cyclic voltammetry was employed to experimentally estimate frontier MO energy levels [17]. Figure 3, (b) depicts a cyclic voltammogram of **10-OPIA** solution recorded at 50 mV/s referenced versus Fc/Fc+ redox couple (in blue). Two tangents were drawn (in red) at the reduction and oxidation parts of the data in order to determine the onsets E_{RED} and E_{OX} on their intersection with the background current tangent. These extracted potentials were employed to evaluate the HOMO and LUMO energy levels of **10-OPIA** using the following relations [17]:

$$E_{HOMO} = -(E_{OX} + 4.4), eV \quad (2)$$

$$E_{LUMO} = -(E_{RED} + 4.4), eV \quad (3)$$

which allows us to estimate E_{LUMO} = −2.5 eV and E_{HOMO} = −5.2 eV. These values look reasonable in regards to the band gap estimated by absorption spectroscopy. Moreover, the HOMO level of −5.2 eV appears to be in good agreement with DFT calculations (Table 1), confirming our initial guess for good affinity of **10-OPIA** material with Au contacts as a p-type semiconductor.

Taking into account the experimental results from cyclic voltammetry, we find the electrochemical band gap energy (E_{HOMO}-E_{LUMO}) E_{gEC} = 2.7 eV to be in good agreement with the

Table 1 Comparison of band gap and MO values of **10-OPIA** between B3LYP/6-31G++(d,p) level of theory (DFT) and electrochemistry (CV).

Method	E_{HOMO} (eV)	E_{LUMO} (eV)	E_g (eV)
DFT	-5.3	-2.0	3.3
CV	-5.2	-2.5	2.7

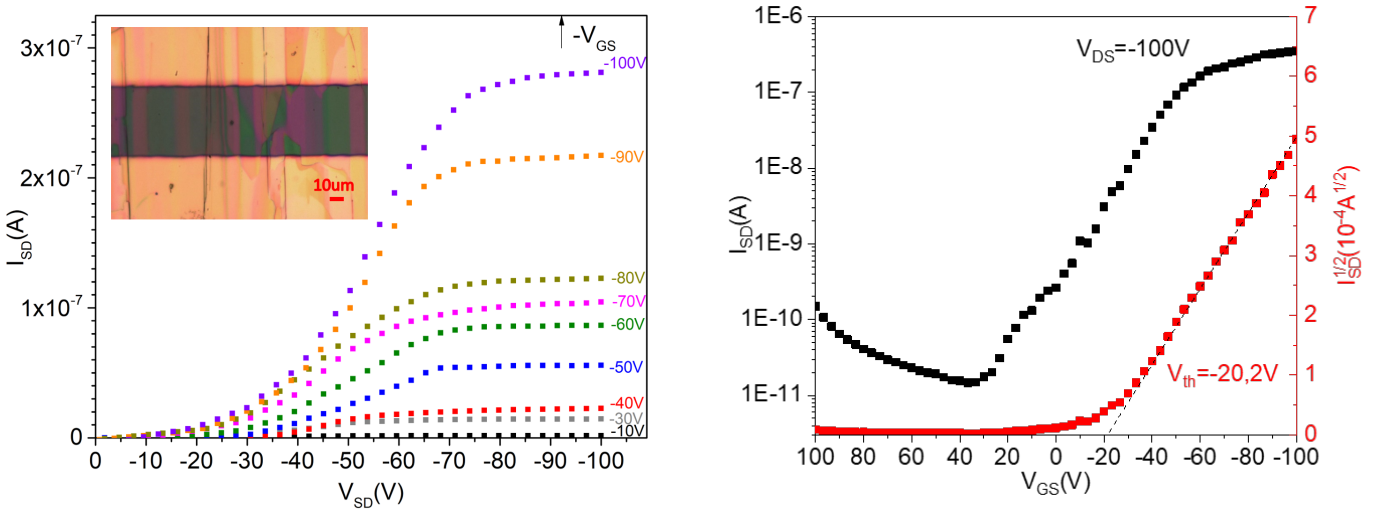

(a) (b)

Fig. 4 (a) Output characteristic of an OFET (L = 50 μm, W=18 mm) prepared with **10-OPIA**. **Inset:** photo of channel region. (b) Transfer characteristic and V_{th} of the same device.

value E_{gO} = 2.7 eV obtained for a thin solid film of **10-OPIA** by absorption spectroscopy. Experimentally obtained HOMO level is in good agreement with its theoretical value, however the energy level of LUMO is noticeably underestimated (about 0.5 eV), which is the reason of band gap energy overestimation.

Cyclic voltammograms of **10-OPIA** recorded at different scanning rates are assembled in Figure 6 of ESI†. It is possible to observe distinct features corresponding to the electrochemical oxidation and reduction of **10-OPIA** molecules. The peak positions are independent to the scanning speed, while the recorded current is proportional to it. The asymmetric profile of oxidation indicates irreversibility of these two processes related to the instability of oxidized/reduced **10-OPIA** species in solution.

Charge transport properties

We have carried out current-voltage measurements on **10-OPIA** OFET in air and at room temperature to characterize the charge transport of this new material. Our deposition technique has allowed us to grow relatively big crystals (greater than channel length) in the direction favorable for charge transport ($\pi-\pi$ stacking plane normal to electrodes).

Inset of Figure 4, (a) shows magnification of transistor channel area in inter-digitated (IE) geometry (L = 50 μm, W = 18mm) with deposited **10-OPIA** thin film, which reveals large crystalline domains crossing both (source and drain) electrodes. The yield of 17 working devices out of 20 per substrate on average was achieved.

The device was characterized in ambient air conditions. The output characteristic of **10-OPIA** OFET in inter-digitated configuration is presented in the Figure 4, (a). This device demonstrates characteristic features of a field-effect transistor: drain-source current is proportional to the negative gate voltage, and the curve has two distinct regions: quasilinear on lower voltage and saturation on higher voltage. Field effect hole mobility is calculated from the saturation part of the drain-source current: $\mu = (2.6 \pm 1.2) \times 10^{-5}\,\mathrm{cm}^2/(\mathrm{V\,s})$. Mobility values extracted for devices in linear configuration (L = 30 μm, W = 1mm) showed slightly higher hole mobility $\mu = (4.1 \pm 2.7) \times 10^{-5}\,\mathrm{cm}^2/(\mathrm{V\,s})$ (output and transfer characteristics of linear OFET can be found in Figure 11 of ESI†). We may speculate that longer channel (50 μm vs 30 μm) results in higher amount of structural micro-defects in **10-OPIA** layer, which may be responsible for lower average mobility.

The hole mobility value is comparable to that obtained by Chung *et al.*[7] for symmetrical 9,10-TIPS functionalized antracene derivatives substituted in 2,6- positions with phenylene vinylene ($\mu = (5.21 \pm 3.55) \times 10^{-5}\,\mathrm{cm}^2/(\mathrm{V\,s})$) and hexyl thiophene ($\mu = (2.05 \pm 1.17) \times 10^{-6}\,\mathrm{cm}^2/(\mathrm{V\,s})$) in thin film form. It should be noted that these reported results were obtained for devices in bottom gate/top contact (BGTC) configuration, which usually exhibits better results[18] than that of bottom gate/bottom contact geometry (used in this work). It is also of interest to compare μ_{hole} of **10-OPIA** to other asymmetrical anthracene derivatives. Recently, F. Qiu *et al.*[19] provided a comparative study where they have varied the linkage between the phenyl and anthracenyl moieties. It was demonstrated that for thermally evaporated polycrystalline films in BGTC configuration the hole mobility varied between 0.89 $\mathrm{cm}^2/(\mathrm{V\,s})$ for vinyl and $5.56 \times 10^{-5}\,\mathrm{cm}^2/(\mathrm{V\,s})$ for ethynyl linkage. Single crystal OFET mobilities for these materials accounted only for one order of magnitude difference between these two materials, which indicates the profound influence of molecular geometry on the bulk material behaviour. For **10-OPIA**, torsion between phenyl and anthracenyl moieties may result in inter-molecular packing which is less optimal for charge transport. That is in contrast with 2-(phenylvinyl)anthracene based molecule characterized by A. Dadvand *et al.*[20], even though these two molecules have isoelectronic π-conjugated core.

Performance of OFETs is typically affected by high contact re-

sistance related to imperfect injection of charge carriers into the channel. It is well known that even closely matched ϕ of contact material and MO level as in the case of Au/pentacene may exhibit substantial (0.6 eV) hole injection barrier[21]. Additional steps may be implemented to decrease contact resistance such as contact functionalization with SAMs or deposition of oxide interlayer[22] to tune metal work function[18] for optimal hole injection.

The transfer characteristic and threshold voltage of **10-OPIA** OFET in linear configuration are presented in the Figure 4, (b). Transfer characteristic allows us to extract the ON/OFF ratio (10^4) of the device. The threshold voltage for this device is found to be -20.2 V (-27.6 V in linear configuration). We would like to underline a relatively low threshold voltage obtained with **10-OPIA** material for this fabrication method (drop casting), which in some cases may be greater than -50 V[23].

Interestingly, thermal annealing of devices did not result in improvement of carrier mobility, but in contrary it dramatically degraded their performance: by examining the substrates under optical microscope, we have found that annealing on temperatures above 80 °C results in apparition of significant amount of cracks in the channel area, which act as structural defects and impede charge transport.

Photoconductive properties

During the initial testing of devices fabricated with **10-OPIA**, we have noticed pronounced photosensitivity of **10-OPIA** material to 3300K light. To further investigate this phenomena, we have employed a 455 nm (bandwidth FWHM = 18 nm) light source (variable power LED) which corresponds to the edge of absorption for **10-OPIA** in a solid film form (inset of Figure 3, a).

Figure 5 represent the transfer characteristic of previously described OFET device under irradiation of varying power density. We would like to underline how the current I_{SD} is amplified by incident light, while retaining distinct ON and OFF states.

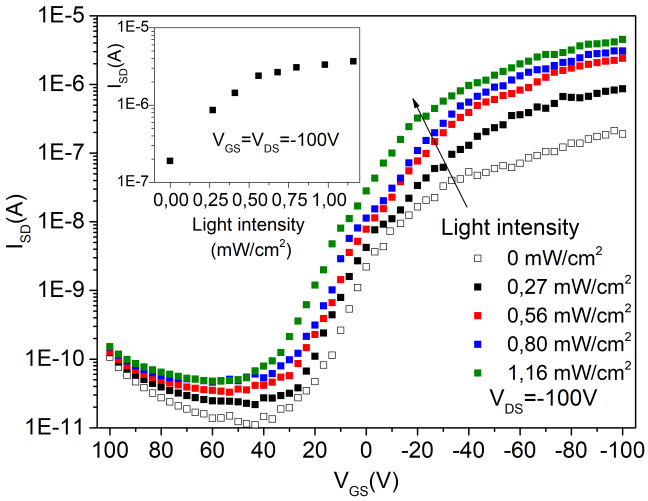

Fig. 5 Plot of transfer characteristic of an OFET prepared with **10-OPIA** for different illumination intensities. Illumination wavelength is λ=455 nm, V_{SD} = -100V. **Inset:** Plot of saturation drain-source current as a function of light intensity.

In addition to conventional parameters (field effect mobility, threshold voltage, ON/OFF ratio), phototransistors are characterized by two additional parameters: photosensitivity P (ratio of photocurrent to dark current) and responsivity R (factor of proportionality of photocurrent to incident light power). We present these parameters in the Figure 6, (a). It is of interest to notice how responsivity gradually increases with negative gate voltage and follows the transfer characteristic of OFET. This parameter exceeds 1 A/W at higher gate voltages, which may be considered reasonably high when compared to typical organic materials[24,25] and even some inorganic semiconductors[26]. Symmetrical anthracene derivative studied by Li *et al.*[27] demonstrated responsivity between 1 and 10 A/W in the form of poly-crystalline thin film. Single crystal devices generally demonstrate much higher performance, as in the case of alkyl-thienothiophene-substituted anthracene[28] where responsivity exceeded 3000 A/W.

The photosensitivity of this device is found to be maximal at intermediate gate voltage, which is directly related to a significant decrease of threshold voltage under illumination due to photogating effect (from V_{th} = -20.2V to +20.3V), and decreases on higher gate field values (where I_{SD} increases in dark conditions), stabilizing around 100. This may be explained by taking into account that the process of photoexcitation is somewhat similar to the field effect in regard to the increase in local density of charge carriers. The more than two order increase observed for current amplitude may indicate filling of significant amount of trap states by photogenerated carriers. In cooperation with field effect it may bring the device closer to the regime where the source-drain current becomes contact-limited[29]. Visible saturation of I_{SD} as a function of illumination power (inset of Figure 5) confirms this observation.

It is of interest to compare this behavior with the work published by Pal *et al.*[30], where a field effect transistor prepared with poly(3-hexylthiophene) (P3HT) in bottom gate/bottom contact configuration showed high performance under illumination. The ON/OFF ratio degraded significantly upon illumination (about 2 orders) which is in distinct contrast with our case. For **10-OPIA** OFET, the ON/OFF ratio upon illumination is found to be almost unchanged from dark conditions (around 10^4) even on relatively high illumination power (greater than 1 mW/cm^2, Figure 12 of ESI†) which may indicate a relatively high recombination barrier for photogenerated electrons. A larger band gap of **10-OPIA** (as compared to that of P3HT) allows this device with Au electrodes to retain its p-channel character even upon significant illumination ("photo-doping"). Another possible explanation involves substantial difference between electron and hole mobilities in the bulk of **10-OPIA**, which limits the number of photogenerated electrons participating in the channel current. This may explain large photoinduced gain of OFET's transfer curve on the majority of gate voltage range.

Persistent photoconductivity

Before we continue our investigations of photoconductive properties of **10-OPIA**, it is necessary to explain the nature of this large photoconductive gain. As we have mentioned, subjection of **10-OPIA** to incident light results in the increase of channel con-

ductivity (photoconductive effect) and threshold voltage reduction (photogating effect): (i) Incident light creates electron-hole pairs in the semiconductor, which become separated under applied electric field V_{DS} and participate in the increase of source-drain current (Figure 13 of ESI†). This effect is responsible for conductivity boost and positive photocurrent. (ii) Photogating effect is responsible for the aforementioned change of the threshold voltage upon illumination (inset of Figure 6). This effect is explained by the presence of trap states such as structural defects on **10-OPIA**/SiO_2 interface, for example (on the edge of LUMO "band" in the Figure 13 of ESI†, which become populated upon irradiation). The contribution of these charged states acts as an additional local "gate" electric field and is able to noticeably shift the threshold voltage of a device[31], especially if we take into account weak field screening in the bulk of material due to its organic nature.

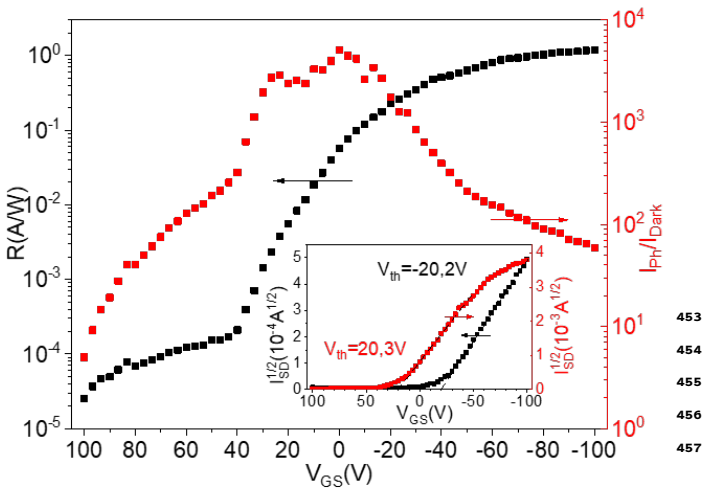

Fig. 6 Plot of photoresponsivity as a function of gate voltage (V_{SD} = -100V) at incident power 1.44 mW/cm^2 (black squares) and photosensitivity (photocurrent to dark current ratio, in red) measured for an OFET in inter-digitated configuration. **Inset:** Threshold voltage of the same device in dark (black squares) conditions and under irradiation (red squares).

The resulting photoconductive gain G is expressed by following equation[29]:

$$G = \frac{c\tau_{pc}}{\tau_{tr}} = \frac{c\tau_{pc}\mu V}{L^2}, \quad (4)$$

where τ_{pc} is the lifetime of photogenerated charge carriers, τ_{tr} is the transit time, c is the concentration of successfully dissociated into electrons and holes light-induced excitons, μ is the mobility of majority carriers, V is the applied voltage and L is the distance between two electrodes. In the case of photogating, the τ_{pc} is limited by the recombination of carriers residing in the trap states.

Field effect dependency of persistent photoconductivity

We have performed transient photoconductivity measurements in order to better understand the recombination behavior of these "gating" states, which has led us to another interesting property of **10-OPIA** - persistent photoconductivity (PPC): sample exhibits higher conductivity in dark condition after being irradiated with light. Figure 7 serves to illustrate this phenomena: the sample is illuminated for 180 s with 1.16 mW/cm^2 of 455 nm light, which yields higher dark current after the light source is turned off as compared to initial dark state.

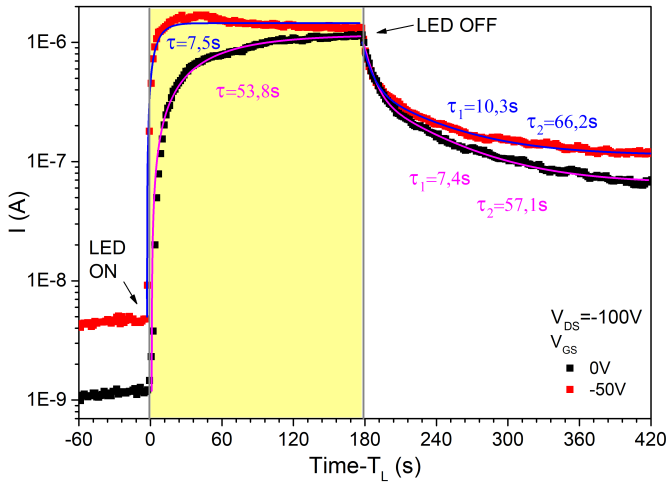

Fig. 7 Plot for current as a function of time. V_{DS} = -50V, V_{GS} = 0V (black symbols), V_{GS} = -50V (red symbols). T_L - start of illumination.

Interestingly, gate bias has pronounced effect on the transient photoconductivity. We have noticed that photo-OFET reacts significantly faster while the gate is being negatively biased than in unbiased state. Photocurrent increase may be fitted with a single exponential growth function:

$$I = I_0\left[1 + \exp\left(\frac{t - t_0}{\tau}\right)\right], \quad (5)$$

where I_0 is the initial current (vertical offset), t_0 is the horizontal offset, and τ is the response time. Application of moderate voltage (V_{GS} = -50V) results in almost one order decrease of saturation time for the photocurrent (7.5s vs 53.8s). This result may be attributed to faster filling of trap states with photogenerated carriers, as well as improved exciton dissociation on the semiconductor/dielectric interface.

The decay part of PPC is affected by gate bias as well. It can be fitted with double exponential decay function:

$$I = I_0 + I_1\exp\left(-\frac{t - t_0}{\tau_1}\right) + I_2\exp\left(-\frac{t - t_0}{\tau_2}\right), \quad (6)$$

where $I_{1,2}$ are the pre-exponential factors and $\tau_{1,2}$ are the relaxation times. It appears that in our case persistent dark current has two components: a fast and a slow relaxation time. This behavior is encountered in polycomponent[32–34] as well as pure materials[35]. Some researches attribute the existence of two decay time components to two different energy levels of trap states: deeper traps are considered to recombine slower[26,36], contrary to more shallow trap states. Some materials show PPC decay with single exponential component, as perylene tetracarboxylic diimide (PTCDI)[37]. Similarly to photocurrent growth, the decay

of PPC is demonstrates its dependence on gate bias. By comparing the extracted relaxation times (Figure 7) we find that the sample under continued negative V_{GS} shows slightly slower current decay (τ_1=10.3s vs 7.4s, τ_2 = 66.2s vs 57.1s). We have also noticed that positive gate bias has detrimental effect on PPC, as the measured current reverts to values similar to the state before irradiation. To better understand these experimental results, we should consider the following: (i) As demonstrated for photocurrent growth, current saturates significantly faster under negative gate voltage, which for same duration of illumination may result in higher occupancy ratio of persistent states. Prolonged periods of illumination have also shown noticeable increase in both time components of current decay, which supports this suggestion. (ii) The gate bias seemingly improves charge separation on the semiconductor/dielectric interface or even allow the photogenerated charge carriers to access energy states which are unavailable at V_{GS}=0V, due to band bending. This delays the recombination of populated trap states, thus increasing their lifetime.

Temperature dependency of PPC

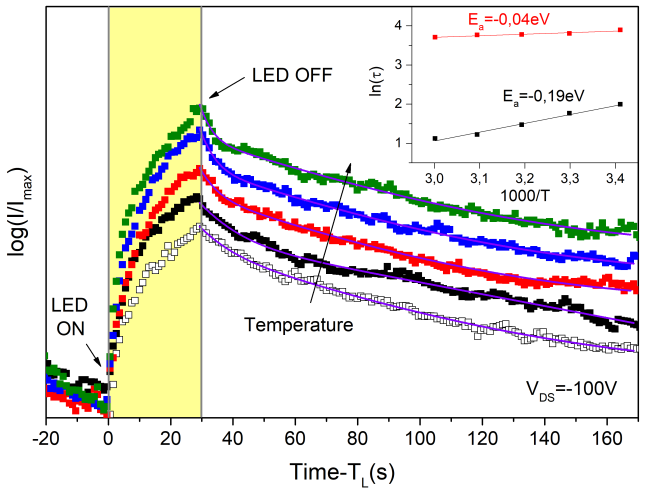

Fig. 8 Plot for normalized photocurrent as a function of time and temperature. Vertical offset is introduced for clarity. V_{SD} = -100V, V_{GS} = 0V. Purple lines represent double exponential fit. T_L - start of illumination. **Inset:** Arrhenius plot of persistent conductivity decay time component. Black squares correspond to τ_1, red squares correspond to τ_2.

In order to investigate the difference between trap state energy levels which we have encountered in PPC decay, we have performed another series of experiments where we have measured the PPC decay time components as a function of temperature. We have performed measurements in a temperature range from 20 °C to 60 °C. Figure 8 assembles transient current plots for different temperatures. Every measurement was preceded by 5s pulse of positive gate voltage (V_{GS}=50V) which is sufficient to "erase" persisting photoconductive states. Current was measured during 30s of illumination, then additional 140s of current decay were recorded. The data was then normalized in respect to the peak photocurrent and the decay part was fitted with the equation 5. The extracted decay time components are assembled in the Table 2. The exponential PPC decay times increase as the temperature decreases. However, it seems that faster decay component τ_1 is affected stronger than the slower τ_2. Tokumoto *et al.*[35] have performed investigations on TIPS-functionalized pentacene, which exhibited similar persistent photoconductivity properties. As in our case, PPC decay time was found to be inversely proportional to the temperature. However, this dependency was found to be more pronounced in the case of TIPS-pentacene than in the case of **10-OPIA**. This may be explained by relatively low energy trap states in a semiconductor with a smaller bad gap (about 1.9 eV for TIPS-pentacene versus 2.7 eV for **10-OPIA**).

Table 2 Time components extracted from data presented in Figure 8.

Temperature (°C)	τ_1 (s)	τ_2 (s)
20	6.7	49.1
30	5.8	44.5
40	4.4	43.7
50	3.4	43.1
60	3.1	41.6

We have calculated activation energy E_a from Arrhenius plot for both decay time components (inset of Figure 8). The extracted value for fast decay component ($E_a(\tau_1)$=0.19 eV) is fives times greater than for slow decay component ($E_a(\tau_2)$=0.04 eV). The value of $E_a(\tau_1)$ is slightly larger than that extracted for PTCDI[37] (E_a=0.14 eV).

Direct comparison of these two time components allows us to conclude that slower decay component τ_2 is indeed connected to deeper trap states,which energetic disorder is less affected by

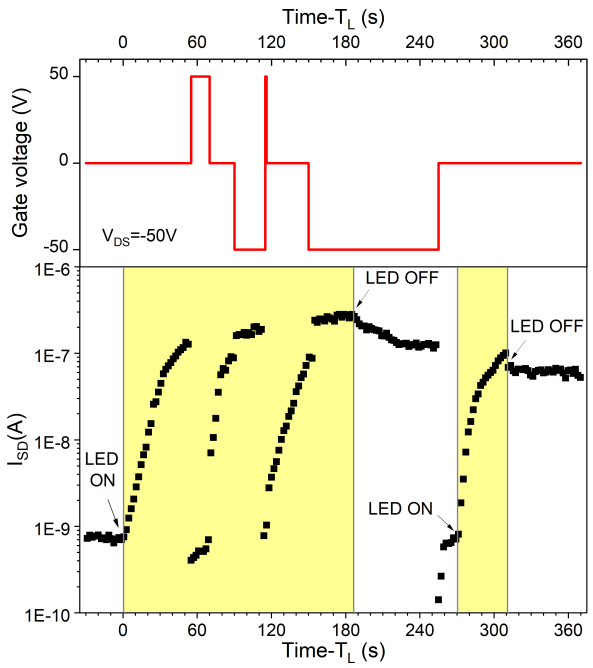

Fig. 9 Plots for OFET channel current (bottom) and gate voltage (top) as a function of time. Irradiation power was 1.16 mW/cm^2 at 455nm. T_L - start of illumination.

temperature increase, as compared to traps characterized by τ_1 (their shallow energy level allows thermal detrapping) [38].

The presence of these deep trap states allows us to propose some thermal stability of photoconductive properties, which may be exploited in potential applications of **10-OPIA** material. In combination with the flexibility of device response with respect to gate voltage, we may propose use of this material in phototransistors (pronounced photoresponsivity $R \sim 1$ A/W and photogating effect), photodetectors and optoisolators (response time may be reduced with smaller channel length and higher gate bias) and memory devices (long persistent photoconductivity decay times, positive gate voltage "erases" persistent state).

Figure 9 demonstrates the channel current plot as a function of time, illumination and gate voltage. The device is initially illuminated at zero gate bias, and the current begins to rise relatively slowly. After 50 seconds, positive voltage (V_{GS}=50V) is applied, which results in immediate breakdown of photocurrent to values below initial (before illumination). We restore zero gate bias after 20 seconds, which allows current amplitude to recover in the same manner as in the beginning of illumination. After 85 seconds under light, we apply negative gate bias (V_{GS}=-50V), which results in immediate saturation of photocurrent. 30 seconds later, short pulse (1s) of positive voltage is applied, which resets the photocurrent in a similar manner. After the recovery of photocurrent, the gate is once again turned to -50V, however this time we let the photocurrent saturate for 30 seconds and then turn off the LED in order to observe decay of persistent photoconductivity. After about one minute we remove gate bias (V_{GS}=0V), which to our surprise acts similarly to application of positive field - the persistent photoconductivity effect is removed. Further part of the plot demonstrates persistent effect in absence of gate voltage modulation.

4 Conclusion

In this work we have described a novel semiconducting material, from synthesis to possible application. The incorporation of heteroatom (nitrogen) in π-conjugated system of this new molecule makes it easier to synthesize, since no carbon-carbon bonds need to be formed when being prepared from commercial precursors. The resulting substance is air-stable, which is an important advantage over classic semiconducting materials based on polyacenes.

We have employed optical spectroscopy and cyclic voltammetry to characterize frontier molecular orbital energy levels as well as band gap energy. Favorable HOMO level of **10-OPIA** allowed us to prepare a p-type transistor. We have developed a simple protocol of deposition for **10-OPIA**, which has allowed us to prepare OFETs in bottom gate/bottom contact configuration, as well as to control preferable direction of crystal growth.

Finally, we have characterized photoconductive properties of this material. We have encountered large photoconductive gain (~ 100) and photoresponsivity ($R \sim 1$ A/W) for OFETs based on **10-OPIA** despite relatively high channel length ($50\,\mu$m). These devices have also demonstrated non-negligible photogating effect which in connection to remarkable control of over photoconductivity via gate bias allows us to suggest further investigations of this new class of materials in relation to photosensitive applications.

Conflicts of interest

The authors declare that there is no conflict of interest regarding the publication of this article.

Acknowledgment

The authors acknowledge financial support of ULCO, Région Hauts-de-France and Collège Doctoral Lille Nord de France. KK is thankful to Amaury Kasprowiak from ULCO for his help with optical spectroscopy and Pr. Dan Scutaru from Technical University of Iasi for helpful discussions.

Notes and references

1 C. Wang, H. Dong, W. Hu, Y. Liu and D. Zhu, *Chemical Reviews*, 2012, **112**, 2208–2267.

2 M. Chen, L. Yan, Y. Zhao, I. Murtaza, H. Meng and W. Huang, *Journal of Materials Chemistry C*, 2018, **6**, 7416–7444.

3 J. Liu, H. Zhang, H. Dong, L. Meng, L. Jiang, L. Jiang, Y. Wang, J. Yu, Y. Sun, W. Hu and A. J. Heeger, *Nature Communications 2015 6*, 2015, **6**, 10032.

4 J. Li, K. Zhou, J. Liu, Y. Zhen, L. Liu, J. Zhang, H. Dong, X. Zhang, L. Jiang and W. Hu, *Journal of the American Chemical Society*, 2017, **139**, 17261–17264.

5 K. Ito, T. Suzuki, Y. Sakamoto, D. Kubota, Y. Inoue, F. Sato and S. Tokito, *Angewandte Chemie - International Edition*, 2003, **42**, 1159–1162.

6 H. Meng, F. Sun, M. B. Goldfinger, G. D. Jaycox, Z. Li, W. J. Marshall and G. S. Blackman, *Journal of the American Chemical Society*, 2005, **127**, 2406–2407.

7 D. S. Chung, J. W. Park, J. H. Park, D. Moon, G. H. Kim, H. S. Lee, D. H. Lee, H. K. Shim, S. K. Kwon and C. E. Park, *Journal of Materials Chemistry*, 2010, **20**, 524–530.

8 K. Kondratenko, D. Singh, Y. Boussoualem, R. Douali, C. Legrand and A. Daoudi, *Journal of Molecular Liquids*, 2019, **276**, 27–31.

9 S. Méry, D. Haristoy, J.-F. Nicoud, D. Guillon, H. Monobe and Y. Shimizu, *J. Mater. Chem.*, 2003, **13**, 1622–1630.

10 K. Kondratenko, Y. Boussoualem, D. P. Singh, R. Visvanathan, A. E. Duncan, N. A. Clark, C. Legrand and A. Daoudi, *Physical Chemistry Chemical Physics*, 2019, **21**, 18686–18698.

11 Y. Chen, C. Li, X. Xu, M. Liu, Y. He, I. Murtaza, D. Zhang, C. Yao, Y. Wang and H. Meng, *ACS Applied Materials & Interfaces*, 2017, **9**, 7305–7314.

12 A. N. Bourque, S. Dufresne and W. G. Skene, *Journal of Physical Chemistry C*, 2009, **113**, 19677–19685.

13 C. J. Yang and S. A. Jenekhe, *Chemistry of Materials*, 1991, **3**, 878–887.

14 M. J. Frisch, G. W. Trucks, H. B. Schlegel, G. E. Scuseria, M. A. Robb, J. R. Cheeseman, G. Scalmani, G. V. Barone, A. Petersson, H. Nakatsuji, X. Li, M. Caricato, A. V. Marenich, J. Bloino, B. G. Janesko, R. Gomperts, B. Mennucci, H. P. Hratchian, J. V. Ortiz, A. F. Izmaylov, J. L. Sonnenberg, D. Williams-Young, F. Ding, F. Lipparini, F. Egidi, J. Goings, B. Peng, A. Petrone, T. Henderson, D. Ranasinghe, V. G. Zakrzewski,

J. Gao, N. Rega, G. Zheng, W. Liang, M. Hada, M. Ehara, K. Toyota, R. Fukuda, J. Hasegawa, M. Ishida, T. Nakajima, Y. Honda, O. Kitao, H. Nakai, T. Vreven, K. Throssell, J. A. Montgomery, J. E. Peralta, F. Ogliaro, M. J. Bearpark, J. J. Heyd, E. N. Brothers, K. N. Kudin, V. N. Staroverov, T. A. Keith, R. Kobayashi, J. Normand, K. Raghavachari, A. P. Rendell, J. C. Burant, S. S. Iyengar, J. Tomasi, M. Cossi, J. M. Millam, M. Klene, C. Adamo, R. Cammi, J. W. Ochterski, R. L. Martin, K. Morokuma, O. Farkas, J. B. Foresman and D. J. Fox, *Gaussian 16, Revision A.03*, 2016.

15 R. R. Gagne, C. A. Koval and G. C. Lisensky, *Inorganic Chemistry*, 1980, **19**, 2854–2855.

16 J. Yoshino, N. Kano and T. Kawashima, *Dalton Transactions*, 2013, **42**, 15826–15834.

17 J. L. Brédas, R. Silbey, D. S. Boudreaux and R. R. Chance, *Journal of the American Chemical Society*, 1983, **105**, 6555–6559.

18 C. Liu, Y. Xu and Y. Y. Noh, *Materials Today*, 2015, **18**, 79–96.

19 F. Qiu, Y. Dong, J. Liu, Y. Sun, H. Geng, H. Zhang, D. Zhu, X. Shi, J. Liu, J. Zhang, S. Ai and L. Jiang, *Journal of Materials Chemistry C*, 2020, **8**, 6006–6012.

20 A. Dadvand, A. G. Moiseev, K. Sawabe, W.-h. Sun, B. Djukic, I. Chung, T. Takenobu, F. Rosei and D. F. Perepichka, *Angewandte Chemie - International Edition*, 2012, **51**, 3837–3841.

21 S. Li, D. Guérin and K. Lmimouni, *Microelectronic Engineering*, 2018, **195**, 62–67.

22 C. M. Kang, Y. Hong and C. Lee, *Japanese Journal of Applied Physics*, 2010, **49**, 3–7.

23 L. Mazur, A. Castiglione, K. Ocytko, F. Kameche, R. Macabies, A. Ainsebaa, D. Kreher, B. Heinrich, B. Donnio, S. Sanaur, E. Lacaze, J. L. Fave, K. Matczyszyn, M. Samoc, J. W. Wu, A. J. Attias, J. C. Ribierre and F. Mathevet, *Organic Electronics: physics, materials, applications*, 2014, **15**, 943–953.

24 M. Hamilton, S. Martin and J. Kanicki, *IEEE Transactions on Electron Devices*, 2004, **51**, 877–885.

25 K. S. Narayan and N. Kumar, *Applied Physics Letters*, 2001, **79**, 1891–1893.

26 A. Di Bartolomeo, L. Genovese, T. Foller, F. Giubileo, G. Luongo, L. Croin, S. J. Liang, L. K. Ang and M. Schleberger, *Nanotechnology*, 2017, **28**, 214002.

27 A. Li, L. Yan, M. Liu, I. Murtaza, C. He, D. Zhang, Y. He and H. Meng, *Journal of Materials Chemistry C*, 2017, **5**, 5304–5309.

28 Y. J. Jang, B. T. Lim, S. B. Yoon, H. J. Choi, J. U. Ha, D. S. Chung and S. G. Lee, *Dyes and Pigments*, 2015, **120**, 30–36.

29 I. H. Campbell and B. K. Crone, *Journal of Applied Physics*, 2007, **101**, 2–7.

30 T. Pal, M. Arif and S. I. Khondaker, *Nanotechnology*, 2010, **21**, 325201.

31 M. Buscema, J. O. Island, D. J. Groenendijk, S. I. Blanter, G. A. Steele, H. S. Van Der Zant and A. Castellanos-Gomez, *Chemical Society Reviews*, 2015, **44**, 3691–3718.

32 F. Yan, J. Li and S. M. Mok, *Journal of Applied Physics*, 2009, **106**, 074501.

33 Z. Sun, J. Li and F. Yan, *Journal of Materials Chemistry*, 2012, **22**, 21673–21678.

34 C. Xie, P. You, Z. Liu, L. Li and F. Yan, *Light: Science & Applications*, 2017, **6**, e17023–e17023.

35 T. Tokumoto, J. Brooks, D. Graf, E. Choi, N. Biskup, D. Eaton, J. Anthony and S. Odom, *Synthetic Metals*, 2005, **152**, 449–452.

36 M. M. Hasan Farooqi and R. K. Srivastava, *Journal of Alloys and Compounds*, 2017, **691**, 275–286.

37 N. Wu, C. Wang, P. M. Slattum, Y. Zhang, X. Yang and L. Zang, *ACS Energy Letters*, 2016, **1**, 906–912.

38 V. Coropceanu, J. Cornil, D. A. da Silva Filho, Y. Olivier, R. Silbey and J. L. Brédas, *Chemical Reviews*, 2007, **107**, 926–952.